Journal of Materials Chemistry A

ROYAL SOCIETY OF CHEMISTRY

PAPER

View Article Online
View Journal | View Issue

Cite this: J. Mater. Chem. A, 2022, 10, 12168

Multi-cavity carbon nanofiber film decorated with Co-N_x doped CNTs for lithium–sulfur batteries with high-areal-capacity†

Xiao-Fei Yu, Bin He, Wen-Cui Li, Tao Wu, Xin-Rong Chen and An-Hui Lu *

The severe shuttle effect and sluggish redox kinetics are the main challenges in sulfur cathodes, leading to capacity degradation and poor rate performance of lithium–sulfur batteries, especially under high sulfur loading and low electrolyte/sulfur (E/S). Herein, a three-dimensional (3D) multi-cavity carbon nanofiber film decorated with Co-N_x doped carbon nanotubes (Co-NCNTs@CNF) has been designed and endowed with dual functions as the sulfur host and an interlayer simultaneously. The multi-cavity structure of Co-NCNTs@CNF provides enough space for high-loading sulfur and relieves the volume expansion of sulfur. *In situ* protruded CNTs and CNF form a conductive framework conducive to accelerating the electrons/ions transfer. The macroporous structure caused by the introduction of Co-containing hydrotalcite is beneficial for electrolyte penetration, thereby reducing the E/S. Co-N_x sites can act as high-efficiency adsorbents and catalysts to adsorb polysulfides and catalyze the conversion of polysulfides rapidly. Owing to the synergistic effect, the Co-NCNTs@CNF-0.42-S cathode with an interlayer delivers a high areal capacity of 4.77 mA h cm^{-2} at 0.2C after 100 cycles under the sulfur loading of 6.7 mg cm^{-2} and E/S = 10 μL mg^{-1}. This strategy provides a new insight for preparing sulfur cathode materials that can work at low E/S under high sulfur loading.

Received 8th April 2022
Accepted 19th May 2022

DOI: 10.1039/d2ta02844a

rsc.li/materials-a

Introduction

Lithium–sulfur (Li–S) batteries have been considered one of the most promising next-generation rechargeable devices due to their high theoretical energy density (~2600 W h kg^{-1}) and abundant sulfur resources.[1,2] Nevertheless, the practical application of Li–S batteries is impeded by several challenging issues, *e.g.*, the inferior electroconductivity of sulfur and discharging products (Li_2S/Li_2S_2), significant volume expansion (80%) of sulfur, and shuttle effect caused by the diffusion of lithium polysulfides (LiPSs) into ether electrolytes.[3,4] These problems can lead to a fast capacity decay, low coulombic efficiency, and poor rate performance, which would be worse under high sulfur loading and lean electrolyte.[5] To address those challenges, a great deal of work has focused on developing novel sulfur hosts to anchor LiPSs and enhance the redox kinetics of sulfur species *via* encapsulating sulfur into conductive carbon[6–8]/polymer[9,10] or metal oxides[11,12]/sulfides[13,14]/nitrides[15,16]/phosphides.[17,18] In addition, unremitting efforts have been made in introducing interlayers[19,20] or modifying separators,[21–24] developing multifunctional binders[25,26] and electrolyte additives.[27–29] However, these modification strategies cannot wholly solve the LiPSs dissolution in electrolytes, especially under high sulfur loading and lean electrolyte. In addition, the slow kinetics of LiPSs conversion to Li_2S_2/Li_2S is an urgent issue to be solved. Therefore, it is essential to prepare a multifunctional sulfur host to accommodate a large amount of sulfur while mitigating volume changes, preventing the shuttle effect, and accelerating redox kinetics of sulfur species.

Recently, researchers have paid attention to the construction of three-dimensional (3D) conductive scaffolds endowed with interlinked channels as sulfur hosts to improve sulfur loading.[30–32] For instance, the Li group developed a 3D hollow carbon nanofiber foam to improve the sulfur loading to 6.2 mg cm^{-2}, which delivers a high areal capacity due to the multiple conductive channels.[33] However, the sulfur particles will expand in volume due to the relatively large size in a single cavity during the discharging process, resulting in the fracture of hollow carbon nanofibers and blockage of electrons/ions transfer channels, which deteriorates the cycle stability of Li–S batteries. Based on the literature, if a single cavity of carbon nanofiber can be divided into multiple small cavities, the internal multi-cavity structure will not only enhance the inner adsorption potential to facilitate the entry of sulfur but also provide a conductive framework to accelerate electrons and ions transfer and increase the utilization of sulfur.[34,35]

Furthermore, the high sulfur loading will aggravate the shuttle effect and reduce the conductivity of the electrode, thereby reducing the sulfur utilization.[36] Therefore, the sulfur

State Key Laboratory of Fine Chemicals, School of Chemical Engineering, Dalian University of Technology, Dalian 116024, P. R. China. E-mail: anhuilu@dlut.edu.cn

† Electronic supplementary information (ESI) available. See https://doi.org/10.1039/d2ta02844a

host needs to be endowed with strong adsorption and catalytic capabilities for LiPSs, and it is also necessary to further enhance the conductivity of the sulfur host. Some researchers usually directly introduce a carbon matrix with good conductivity to compound with the sulfur, *e.g.*, graphene and carbon nanotubes (CNTs),[37,38] which will inevitably increase the contact resistance. According to the literature, the *in situ* co-growth of carbon materials can significantly reduce contact resistance and improve conductivity.[39] Lately, Yu's group has reported an N, O co-doped 3D wood-like carbon framework decorated with CNTs forest, which delivers a capacity of 680 mA h g^{-1} at 1C under a high sulfur loading up to 17.3 mg cm^{-2}.[40] This excellent performance is due to the wood-like framework with CNTs forest, which creates an internal conductive network that provides fast and continuous transfer paths for electrons, ions, and electrolytes.

In addition, the electrolyte/sulfur ratio (E/S), one of the main factors affecting the actual energy density of Li–S batteries, has gradually attracted the attention of researchers. Reducing E/S has become a consensus in practical applications.[41,42] However, once the E/S is too low, the battery will suffer from severe polarization, lowering sulfur utilization. Therefore, to make the battery work normally under lean electrolyte and high sulfur loading, a low-nanoporosity sulfur host with a macroporous structure and high conductivity is preferred,[43] which can guarantee the full wetting of cathodes.[44] For example, Yoshie *et al.* proposed a positive electrode of Li_2S_x held by a sponge of submillimeter-long few-wall CNT that works at low E/S.[45]

In this work, a 3D carbon nanofiber film decorated with Co-N_x doped carbon nanotubes (Co-NCNTs@CNF) has been prepared as the sulfur host and an interlayer. The interior of carbon nanofiber has a multi-cavity structure, providing enough space for high sulfur loading and relieving the volume expansion of sulfur. *In situ* protruded CNTs and CNF can form a conductive framework conducive to accelerating the electrons/ions transfer. Co-containing hydrotalcite as a substrate can promote the growth of long CNTs and increase the mesoporous ratio of Co-NCNTs@CNF, which is beneficial for electrolyte penetration, thereby reducing the E/S. Co-N_x sites can act as efficient adsorbents and catalysts to adsorb polysulfides and promote the transformation of polysulfides. Owing to the synergistic effect, Co-NCNTs@CNF-0.42-S cathode with an interlayer delivers a high areal capacity of 4.77 mA h cm^{-2} at 0.2C after 100 cycles under the sulfur loading of 6.7 mg cm^{-2} and E/S = 10 μL mg^{-1}.

Experimental section

Synthesis of Co-NCNTs@CNF-*x* film

Synthesis of Co-Al LDH. 0.308 g of Al $(NO_3)_3 \cdot 9H_2O$ was dissolved in 300 mL of water. Then 0.720 g of Co $(NO_3)_2 \cdot 6H_2O$ was put into the solution which kept stirring until it dissolved. Next, 2.0 g of hexamine was added, stirring for 30 min. Subsequently, the aqueous solution was transferred to a polytetrafluoroethylene (PTFE) lining, sealed in a stainless-steel vessel, and then heated at 140 °C for 12 h. After cooling down, the olive-green precipitation was washed with water until neutral and dispersed in a 500 mL aqueous solution for later use.

Synthesis of MnO_2 nanowires. A certain mass of $MnSO_4 \cdot H_2O$ was added to 300 mL of water. Then, $KClO_3$, CH_3COOK, and CH_3COOH (16 mL) were added in sequence.[46] After stirring for 5 minutes, the above solution was transferred to a PTFE lining, sealed in a stainless-steel container, and heated at 160 °C for 8 h. After cooling down, the chocolate-colored deposition was washed with deionized water to neutrality and dispersed in a 600 mL aqueous solution.

Synthesis of MnO_2@Co-Al LDH film. A certain amount of the Co-Al LDH and MnO_2 aqueous solution with PVP are mixed under stirring for 2 h. Then, a specific volume of the composite solution was vacuum filtered and washed with water. After drying at 50 °C for 24 h, the MnO_2@Co-Al LDH film was obtained. Thereinto, the volume ratios of Co-Al LDH/MnO_2 were 0, 0.21, 0.42, and 0.84, respectively.

Synthesis of Co-NCNTs@CNF-*x* film. The MnO_2/Co-Al LDH film was placed in a carbonization furnace, using aniline as carbon and nitrogen source, followed by carbonizing at 800 °C for 2 h with a heating rate of 3 °C min^{-1} under Ar atmosphere. Then the carbonized film was soaked in 30 mL 6 mol L^{-1} hydrochloric acid for 3 days, washed with water until neutral, and dried at 50 °C for 24 h to obtain Co-NCNTs@CNF-*x* film. Thereinto, *x* represents 0, 0.21, 0.42, and 0.84, respectively, which corresponds to the volume ratio of Co-Al LDH/MnO_2.

Synthesis of Co-NCNTs@CNF-0.42-S cathodes. The Co-NCNTs@CNF-0.42 film was cut into 12 mm discs. A certain mass of sulfur was dissolved in carbon disulfide (CS_2), forming clear liquor, which was dripped on the discs. After CS_2 volatilizes, the discs were sealed in a vessel and heated at 155 °C for 8 h and then heated to 400 °C for 2 h. After cooling down, the Co-NCNTs@CNF-0.42-S cathode can be obtained. The specific capacity was calculated from the mass of sulfur. For Co-NCNTs@CNF-0.42-S cathode, when the sulfur loading was 2.0, 3.1, 5.6, 6.5, and 6.7 mg cm^{-2}, the corresponding sulfur content was 33, 44, 58, 62, and 63 wt%, respectively. For CP-S cathode, when the sulfur loading was 2.0 and 5.9 mg cm^{-2}, the corresponding sulfur content was 18 and 40 wt%, respectively.

Characterization

Scanning electron microscopy (SEM) analysis was performed on a SU8220 instrument (Hitachi, Japan). HT7700 (Hitachi, Japan) and JEM-F200 (JEOL, Japan) microscopes were used for transmission electron microscopy (TEM) analysis. A Tristar 3000 analyzer (Micromeritics Instruments, USA) was taken to measure N_2 sorption isotherms at 77 K. X-ray photoelectron spectroscopy (XPS) data were collected by an ESCALAB XI+ spectrometer (Thermo Scientific, Britain). X-ray diffraction (XRD) patterns were collected from a PANalytical X'Pert³ powder diffractometer using CuKα radiation (40 kV, 40 mA, $\lambda = 1.54056$ Å). Raman measurements were performed on a DXR Smart Raman spectrometer (Thermo Fisher, America) with a 532 nm laser excitation. An STA 449 F3 analyzer (NETZSCH, Germany) was utilized for thermogravimetric (TG) analysis at a heating rate of 10 °C min^{-1} in an airflow.

Electrochemical measurements

The CR2025 coin-type battery was assembled in an argon-filled glove box, using a Co-NCNTs@CNF-0.42-S disc as a cathode, Li foil as an anode, Celgard 2400 membrane as the separator, and 1 M LiTFSI in DME : DOL (1 : 1, v/v) containing 2 wt% $LiNO_3$ as the electrolyte. When the sulfur loading was 6.7 mg cm^{-2}, the E/S ratio was 10 μL mg^{-1}. Under other sulfur loadings, the E/S ratio was 15 μL mg^{-1}. Galvanostatic discharge–charge (GCD) measurements were operated on a battery tester (Land CT2001A, China) between 1.7 and 2.8 V. Cyclic voltammetry (CV) curves, Tafel plots, and Nyquist plots within a range from 10 mHz to 100 kHz were measured at an electrochemical workstation (CHI660E, China).

In situ XRD and Raman measurements

For *in situ* XRD measurements, Co-NCNTs@CNF-0.42-S (6.0 mg cm^{-2}) as a cathode, an interlayer (Co-NCNTs@CNF-0.21), Li foil as an anode, and glass fiber as a separator (Whatman, GF/D) soaked with electrolytes were assembled into a home-made mold. The *in situ* XRD cell was cycled between 1.7 and 2.8 V at 0.15 A g^{-1} with a Land CT2001A battery test system.

For *in situ* Raman measurements, the sulfur cathode (2.0 mg cm^{-2}), an interlayer, Li foil, and the glass fiber separator soaked with electrolytes were assembled in an *in situ* Raman mold (Tianjin IDA). The electrochemical reaction was utilized by the CV test at a scanning rate of 0.4 mV s^{-1} on a CHI660E electrochemical workstation. The laser irradiated the sulfur cathode through a quartz window of the mold, so the Raman signals of LiPSs in the cathode were collected. Before measuring, the cell was discharged at 1.7 V.

Computational methods

The density functional theory (DFT) calculations were performed using the Vienna *ab initio* simulation package (VASP),[47,48] with the ionic potentials including the effect of core electrons being described by the projector augmented wave (PAW) method.[49,50] The exchange–correlation energy was evaluated using the Perdew–Burke–Ernzerhof (PBE) functional with GGA exchange-correlation (XC).[51,52] The plane-wave kinetic cut-off energy was set as 500 eV, and the total energy convergence was lower than 1×10^{-4} eV, with the force convergence at 0.05 eV $Å^{-1}$ for geometric optimization. The first Brillouin zone was sampled with 5×5 Γ-centred *k*-points grids for all calculations. For the adsorption conformation simulations, we used the vdW-D3 functional to include the physical van der Waals interaction.[53] A vacuum layer of 20 Å thick was used to avoid layer interaction. The structures of CP and Co-NCNTs@CNF-0.42 are modeled based on the supercell of graphene containing 5×5 unit cells.

Results and discussion

The synthetic procedure of three-dimensional (3D) multi-cavity carbon nanofiber film decorated with Co-N_x doped carbon nanotubes (Co-NCNTs@CNF) is described. Firstly, cobalt–aluminum hydrotalcite flakes (Co-Al LDH, Fig. S1a†) and manganese oxide (MnO_2) nanowires were prepared by hydrothermal methods, respectively. After the two were dispersed in an aqueous solution, they were physically combined and then vacuum-filtered to form a film (MnO_2@Co-Al LDH). During the carbonization process, using aniline as a carbon source and nitrogen source, a layer of carbon was deposited on the MnO_2@Co-Al LDH. At the same time, Co^{2+} is reduced to Co nanoparticles, which act as catalysts to promote the growth of CNTs.[54] In addition, MnO_2 is reduced to MnO, followed by acid etching to obtain Co-NCNTs@CNF-*x* film.

The length of MnO_2 nanowires is greater than 50 microns, and the diameter is 100–200 nm (Fig. S1b and c†). Co-Al LDH is uniformly dispersed in the film formed by overlapping MnO_2 nanowires (Fig. S2†). When Co-Al LDH/MnO_2 is 0, MnO_2 nanowires will be transferred to hollow carbon nanofibers (CNF) with a diameter of 200 nm after the CVD process, as shown in Fig. S3.† When the Co-Al LDH/MnO_2 is 0.21, scanning electron microscope (SEM) images of Co-NCNTs@CNF-0.21 are shown in Fig. 1a–c. After carbonization and pickling, the sample maintains the nanofiber structure with a diameter of about 100–200 nm, while slender and curved CNTs with a length of micrometers and a diameter of about 70–100 nm are grown on the surface of the nanofibers. It shows that this method can successfully grow CNTs on the surface of CNF to form a 3D cross-linked conductive network structure. After increasing the volume ratio of Co-Al LDH/MnO_2 from 0.21 to 0.42, the SEM images of Co-NCNTs@CNF-0.42 are shown in Fig. 1d–f. It can be seen that the number of CNTs wound on the surface of the CNF increases, and the diameter becomes finer, about 50–70 nm.

Transmission electron microscope (TEM) images of Co-NCNTs@CNF-0.21 (Fig. 2a and b) show that the carbon nanofiber film has a multi-cavity structure. Some Co nanoparticles are wrapped in the CNTs, indicating that the growth mechanism of the CNTs is the *in situ* top catalytic growth mode of Co nanoparticles. That is to say, the release of reducing gas (CN_x) during the heat treatment in an argon atmosphere can reduce Co^{2+} to metallic Co nanoparticles, which can act as catalysts to adsorb CN_x and promote the growth of CNTs through an *in situ* catalytic growth mechanism.[55] TEM images of Co-NCNTs@CNF-

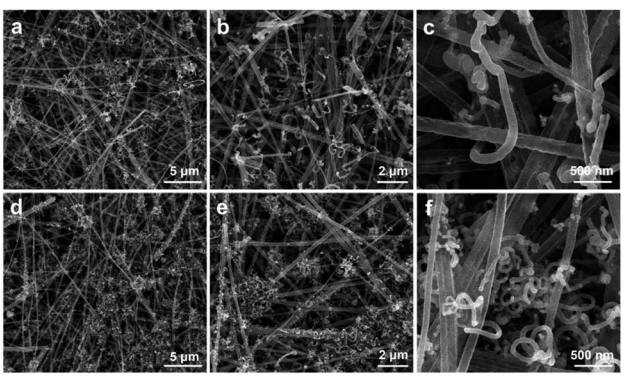

Fig. 1 SEM images of (a–c) Co-NCNTs@CNF-0.21 and (d–f) Co-NCNTs@CNF-0.42.

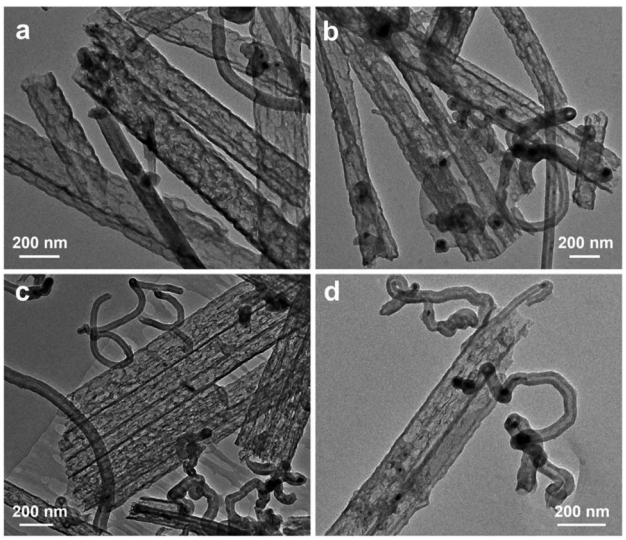

Fig. 2 TEM images of (a and b) Co-NCNTs@CNF-0.21 and (c and d) Co-NCNTs@CNF-0.42.

0.42 (Fig. 2c and d) show that the carbon nanofiber still has a multi-cavity structure, and CNTs are grown on the surface of the CNF. As the content of Co-Al LDH increases, the number of CNTs increases, and the diameter of the CNTs becomes smaller, consistent with SEM results. The multi-cavity structure of carbon nanofiber is mainly due to the removal of MnO and Co nanoparticles by acid etching. When the Co-Al LDH/MnO_2 increases to 0.84, TEM images show the agglomeration of CNTs and CNF (Fig. S4†), indicating that excessive addition of Co-Al LDH is not conducive to even dispersion.

XRD patterns of the Co-Al LDH and MnO_2 (Fig. 3a) synthesized by the hydrothermal method are consistent with the standard cards,[56] respectively, indicating that the Co-Al LDH and MnO_2 were successfully synthesized. The XRD pattern of MnO_2@Co-Al LDH also shows that Co-Al LDH was successfully mixed with MnO_2 nanowires. After the carbonization, MnO_2 was transformed into MnO, as confirmed by the XRD result (Fig. S5†). The Co-NCNTs@CNF-x film was obtained by acid-washing with 6 mol L^{-1} HCl to form a multi-cavity structure. As shown in Fig. 3b and S6a,† the XRD pattern of CNF shows a peak at $2\theta = 26°$, which represents amorphous carbon, while three peaks representing Co nanoparticles (JCPDS No. 89-4307) can be seen in the XRD patterns of Co-NCNTs@CNF-x ($x = 0.21$, 0.42, and 0.84). The peak intensity of amorphous carbon gradually increases with Co-Al LDH content, indicating the growth of CNTs, consistent with TEM results.

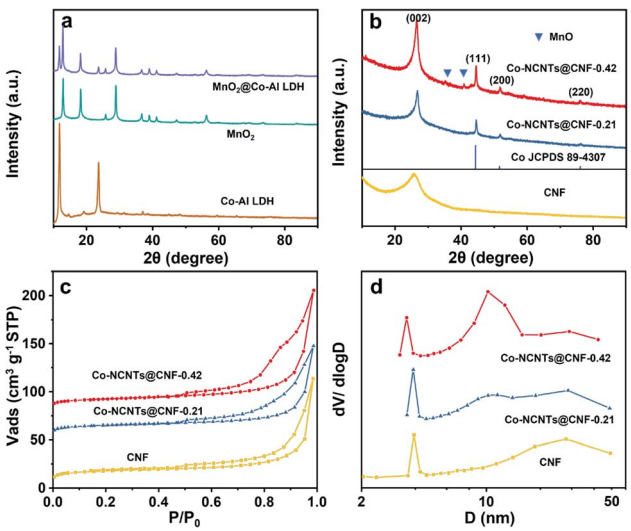

Fig. 3 (a and b) XRD patterns of samples. (c) N_2 sorption isotherms and (d) pore size distributions of CNF and Co-NCNTs@CNF-x samples. The isotherms of Co-NCNTs@CNF-0.21 and Co-NCNTs@CNF-0.42 were vertically offset to 50 and 80 cm^3 g^{-1}, respectively, STP.

The pore structure of Co-NCNTs@CNF-x and CNF were analyzed by nitrogen sorption tests (Fig. 3c and S6b†). The nitrogen sorption isotherms show type II and IV characteristics, a hysteresis loop at $P/P_0 \geq 0.4$, and the adsorption volume increases sharply when P/P_0 is close to 1.0, indicating the existence of mesopores and macropores.[57] The pore structure parameters of Co-NCNTs@CNF-x and CNF are listed in Table S1.† After removing MnO, the specific surface area (S_{BET}) of CNF is 57.8 m^2 g^{-1}, and its pore volume (V_{total}) is 0.18 cm^3 g^{-1}. With the gradual increase of Co-Al LDH content, the S_{micro} and V_{micro} of the samples gradually decrease, and the proportion of mesopores gradually increases. It may be that the rise of Co-Al LDH content leads to the increase of Co nanoparticles. Thus, the cavities are left after etching Co nanoparticles. The pore size distributions (PSDs, Fig. 3d and S6b†) show that the pore size of CNF is concentrated at 29 nm, which may correspond to the pores left after etching MnO. The PSDs of the Co-NCNTs@CNF-x samples are concentrated at 29 nm, which laterally confirms that the size of MnO is 29 nm. In addition, Co-NCNTs@CNF-0.21 and Co-NCNTs@CNF-0.42 both have mesopores at 10 nm, which may correspond to the size of Co nanoparticles. The PSDs of micropores obtained by CO_2 adsorption measurement at 273 K can be seen in Fig. S7.† The micropores are mainly concentrated at ~0.6 and 0.8 nm. The Raman spectra of Co-NCNTs@CNF-x samples (Fig. S8a†) show that the I_D/I_G of Co-NCNTs@CNF-x increases from 1.02 to 1.19 with the rise of Co-Al LDH content, indicating that the addition of Co-Al LDH increases the disorder degree of hybrids. TG curves of Co-NCNTs@CNF-x in airflow are shown in Fig. S8b.† With the increase of Co-Al LDH content from 0 to 0.84, the residual mass of samples is about 3.9, 8.1, 12.1, and 15.8 wt%, respectively. According to TG results, the Co content in Co-NCNTs@CNF-x (x = 0.21, 0.42, and 0.84) is calculated to be about 3.6, 6.5, and 9.3 wt%, respectively.

XPS spectra of Co-NCNTs@CNF-0.42 are displayed in Fig. S9.† The C 1s XPS spectrum can be fitted into four peaks (Fig. S9a†), which are C=C (284.8 eV), C–N (285.4 eV), C=O (286.9 eV), and C–OH (288.1 eV), respectively. As shown in Fig. S9b,† the N 1s XPS spectrum can be resolved into five peaks, located at 398.4, 399.0, 399.7, 401.0, and 404.0 eV, respectively, corresponding to pyridinic N, Co-N_x, pyrrolic N, graphitic N, and oxidized-N.[58] As shown in Fig. S9c,† Co 2p XPS spectra can be fitted into three peaks, which are Co^0 (778.0 eV), Co-N_x (779.5 eV), and Co^{2+} (781.6 eV), respectively.[59] The XPS results

confirmed the presence of Co-N_x sites in Co-NCNTs@CNF-0.42, which have been reported to be highly active sites for many electrocatalytic reactions and anchoring LiPSs.[60–63] To investigate the interaction between the Co-NCNTs@CNF-0.42 and LiPSs, the samples were immersed in 0.001 mol L^{-1} Li_2S_6 solution for 9 h, as shown in Fig. S10.† Compared with carbon paper (CP), the solution colour of Co-NCNTs@CNf-0.42 turned from yellow to transparent. The result shows a strong chemical interaction between the Co-NCNTs@CNF-0.42 and LiPSs.

Co-NCNTs@CNF-0.42-S electrode was obtained from immersing sulfur directly into the electrode by a melt impregnation method. The XRD pattern of Co-NCNTs@CNF-0.42-S (Fig. S11†) shows the characteristic diffraction peaks of monoclinic sulfur, indicating that Co-NCNTs@CNF-0.42 has a strong binding effect on sulfur.[64] The macroscopic picture and SEM images of Co-NCNTs@CNF-0.42-S are displayed in Fig. S12.† After sulfur impregnation, the film maintains the self-standing architecture, and the carbon nanofiber structure interwoven with intruded CNTs is still well-retained. The distribution of sulfur in the electrode was characterized by STEM-EDS. As shown in Fig. S13,† there is no sulfur agglomeration, and sulfur is evenly distributed in the electrode.

The Co-NCNTs@CNF-0.42-S electrode with a Co-NCNTs@CNF-0.21 interlayer was assembled to test the electrochemical performance. CP was cut into discs to load sulfur as a control sample. Cyclic voltammetry (CV) curves of the Co-NCNTs@CNF-0.42-S electrode at the 1st, 3rd, and 5th cycles are exhibited in Fig. 4a, respectively. The reduction peaks at 2.3 and 1.8 V correspond to the reduction of S_8 to higher-order Li_2S_x ($4 \leq x \leq 8$) and the reduction of Li_2S_x to insoluble Li_2S_2/Li_2S, respectively. The oxidation peaks around 2.38 and 2.52 V correspond to the oxidation of Li_2S_2/Li_2S to Li_2S_8 and S_8. The reduction and oxidation peaks are pronounced, indicating that the sulfur host has abundant transport channels for electrons and ions, which leads to a rapid redox reaction. In addition, the 3rd and 5th CV curves almost overlap, indicating that the Co-NCNTs@CNF-0.42-S cathode has good electrochemical reaction reversibility and stability. In contrast, CV curves of CP-S electrode with interlayer are shown in Fig. S14a,† whose oxidation peaks appear about 2.42 and 2.51 V, lagging behind that of Co-NCNTs@CNF-0.42-S electrode. As shown in Fig. 4b, the Nyquist plot is composed of a semicircle in the high-frequency region and a straight line in the low-frequency region. The semicircle reflects the charge transfer resistance (R_{ct}), and the straight line is the Warburg resistance (Z_w), which demonstrates the ion diffusion. After cycles, the semicircle diameter decreased. The inclination angle between the Z_w and the X-axis was greater than 45°, indicating that the R_{ct} decreased, and the ion diffusion rate increased. Nyquist plots of the CP-S electrode after cycles show that the R_{ct} is larger than that of the Co-NCNTs@CNF-0.42-S electrode (Fig. S14b†). This result further proved that Co-NCNTs@CNF-0.42 has good conductivity and provides abundant transfer channels for electrons/ions, contributing to fast electrochemical reactions. The rate performance of Co-NCNTs@CNF-0.42-S and CP-S cathodes was tested at various current densities from 0.2 to 2C (Fig. 4c). At a current density of 0.2, 0.5, 1, and 2C, the

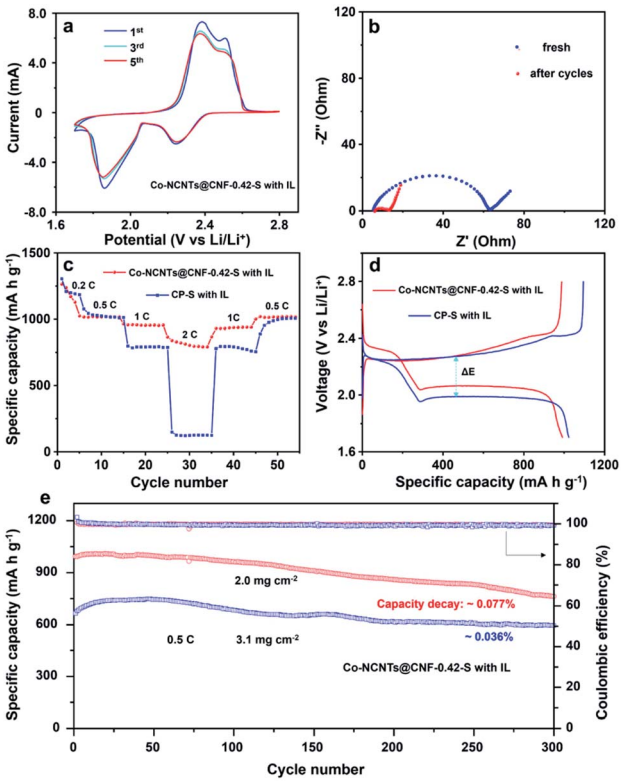

Fig. 4 (a) CV curves at 0.1 mV s^{-1}, (b) Nyquist plots before and after CV tests of Co-NCNTs@CNF-0.42-S electrode with an IL. (c) Rate performance at current densities from 0.2 to 2C and (d) initial discharge and charge curves of Co-NCNTs@CNF-0.42-S and CP-S electrodes with an IL at 0.5C. (e) Cycling performance of Co-NCNTs@CNF-0.42-S electrode with an IL under different sulfur loadings at 0.5C.

discharge capacity of Co-NCNTs@CNF-0.42-S cathode is about 1171, 1018, 954, and 804 mA h g^{-1}, respectively. The specific capacity of Co-NCNTs@CNF-0.42-S cathode at 1 and 2C is higher than that of CP-S cathode (791 and 124 mA h g^{-1}), respectively, which shows a good rate capability of Co-NCNTs@CNF-0.42-S cathode. When the current density returns to 0.5C, the capacity can still return to 1017 mA h g^{-1}, suggesting the combination of Co-NCNTs@CNF-0.42-S cathode and Co-NCNTs@CNF-0.21 interlayer can improve the electrochemical performance. The initial charge–discharge curve of Co-NCNTs@CNF-0.42-S and CP-S electrode combined with the interlayer at 0.5C is shown in Fig. 4d. Two obvious discharging voltage platforms at 2.3 and 2.1 V of the Co-NCNTs@CNF-0.42-S electrode are higher than that of the CP-S electrode. The voltage platforms in the charging curve are concentrated in 2.3–2.5 V, close to the redox peaks in CV curves. When the specific capacity is 420 mA h g^{-1}, the voltage difference (ΔE) of the Co-NCNTs@CNF-0.42-S electrode is smaller than that of the CP-S electrode, indicating that the electrochemical polarization effect is relatively small, mainly attributed to the good electronic conductivity of sulfur host and interlayer, which can reduce the internal resistance of the battery. Additionally, the cycling performance of the Co-NCNTs@CNF-0.42-S electrodes under different sulfur loadings was tested with a larger current density

of 0.5C, as shown in Fig. 4e. When the sulfur loading is 2.0 mg cm^{-2}, the initial specific capacity at 0.5C is 992 mA h g^{-1} after activation at 0.2C and maintains at 763 mA h g^{-1} after 300 cycles with a capacity decay of 0.077%. When the sulfur loading is 3.1 mg cm^{-2}, the capacity is 666 mA h g^{-1} at 0.5C after activation and maintains at 594 mA h g^{-1} after 300 cycles, and the capacity decay is 0.036%, which is lower than that of sulfur loading at 2.0 mg cm^{-2}. The above results indicate that Co-NCNTs@CNF-0.42-S electrode combined with the interlayer can significantly improve the cycle stability of the battery under high sulfur loading.

The cycling performance of Co-NCNTs@CNF-0.42-S and CP-S cathodes with or without an interlayer (Co-NCNTs@CNF-0.21) at 0.2C was tested under high sulfur areal loading conditions, respectively. As shown in Fig. 5a, when the sulfur loading is 6.5 mg cm^{-2}, the first discharge specific capacity of the Co-NCNTs@CNF-0.42-S cathode with the interlayer at 0.2C is 962 mA h g^{-1}, much higher than that of Co-NCNTs@CNF-0.42-S cathode without interlayer (747 mA h g^{-1} with a sulfur loading of 5.6 mg cm^{-2}) and CP-S cathode (318 mA h g^{-1} with a sulfur loading of 5.9 mg cm^{-2}, Fig. S15†). After 100 cycles, the specific capacity of the Co-NCNTs@CNF-0.42-S cathode with the interlayer was 790 mA h g^{-1}, higher than that of the cathode without the interlayer (605 mA h g^{-1}), which indicates that the addition of interlayer can effectively enhance the capacity and cycling performance of the Co-NCNTs@CNF-0.42-S cathode, especially under high sulfur loading. As shown in Table S2,† compared with the literature, the Co-NCNTs@CNF-0.42-S cathode combined with the interlayer showed higher areal specific capacity and better cycling stability. In addition, the capacity loss of CP-S cathode is severe under high sulfur loading, and its capacity is much lower than that of Co-NCNTs@CNF-0.42-S cathode, indicating that Co-NCNTs@CNF-0.42 is more suitable for high sulfur loading. Therefore, the Co-NCNTs@CNF-0.42-S cathode combined with the Co-NCNTs@CNF-0.21 interlayer can significantly boost the electrochemical performance of Li–S batteries.

Except for the high sulfur areal loading parameter, the amount of electrolyte (E/S) is also a very critical parameter. Higher E/S will significantly reduce the actual energy density of the battery, so the E/S has become one of the effective ways to promote Li–S batteries from laboratory to application. When the E/S is 10 μL mg^{-1}, the cycling performance of the Co-NCNTs@CNF-0.42-S electrode combined with the interlayer at 0.2C is shown in Fig. 5b. When the sulfur loading is 6.7 mg cm^{-2}, the first discharge specific capacity of the sulfur cathode is 951 mA h g^{-1}, and an areal specific capacity is 6.37 mA h cm^{-2} at 0.2C, which remains at 712 mA h g^{-1} after 100 cycles with a high areal specific capacity (4.77 mA h cm^{-2}). Therefore, the Co-NCNTs@CNF-0.42-S electrode combined with the Co-NCNTs@CNF-0.21 interlayer exhibits good electrochemical performance even under high sulfur loading and low E/S. The good performance mainly originated from the macroporous structure with high conductivity of Co-NCNTs@CNF-0.42, which can effectively promote electrolyte penetration, thereby reducing the dependence of sulfur cathode on the amount of electrolyte.[44,65]

To investigate the catalytic activity of Co-NCNTs@CNF-0.42, a 2025-type coin-type symmetrical battery was assembled with

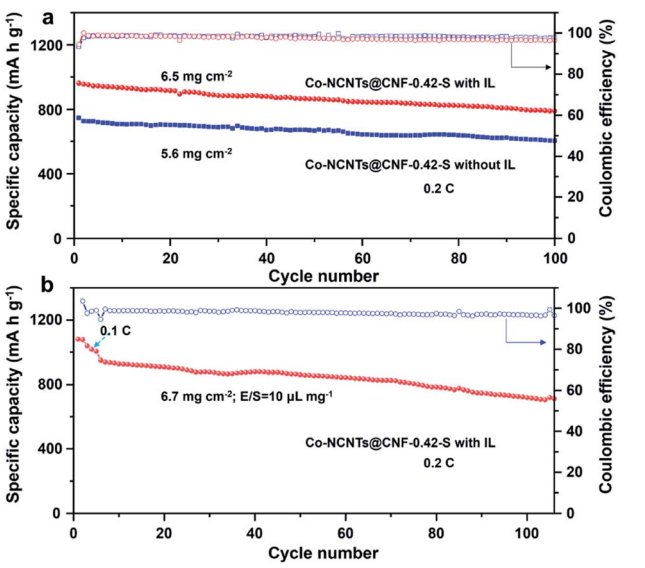

Fig. 5 Cycling performance of Co-NCNTs@CNF-0.42-S electrodes at 0.2C (a) with/without an IL under high sulfur loading and (b) with an IL under high sulfur loading and low E/S.

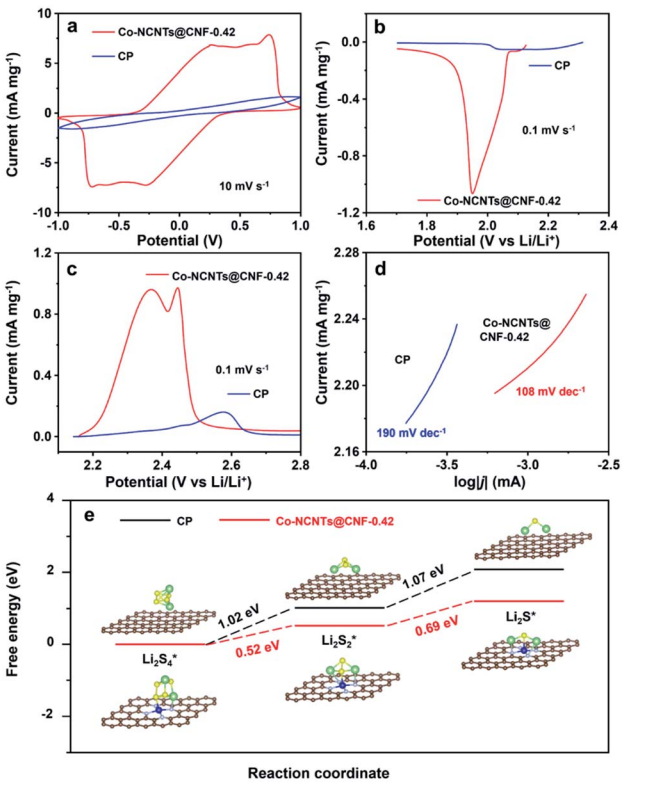

Fig. 6 (a) CV curves of symmetric batteries at a scan rate of 10 mV s^{-1}, (b and c) LSV curves at 0.1 mV s^{-1}, and (d) Tafel plots of Co-NCNTs@CNF-0.42 and CP electrodes. (e) Energy profiles for the reduction of LiPSs on Co-NCNTs@CNF-0.42 and CP substrates. The inset is optimized adsorption conformations of LiPSs on Co-NCNTs@CNF-0.42 and CP substrates.

0.2 M Li_2S_6 to test CV curves and Nyquist plots. CP electrode was used as a contrast sample. As shown in Fig. 6a, a couple of reversible redox peaks can be observed from the CV curve of the Co-NCNTs@CNF-0.42 electrode, indicating that the electrode has good reversibility of the electrochemical reaction. In contrast, no redox peak is observed from the CV curve of the CP electrode, and the current density is lower than that of the Co-NCNTs@CNF-0.42 electrode, indicating that Co-NCNTs@CNF-0.42 has a catalytic effect on Li_2S_6. In addition, the Nyquist plot after cycling (Fig. S16†) also illustrates that the Co-NCNTs@CNF-0.42 electrode has a lower R_{ct} and faster ion transport compared to the CP electrode. To further prove that the Co-NCNTs@CNF-0.42 has a catalytic effect on Li_2S_6, Co-NCNTs@CNF-0.42 as the cathode, the Li foil as the anode, and 0.2 M Li_2S_6 as the electrolyte were assembled to test linear sweep voltammetry (LSV) curves and Tafel plots. When the voltage window varies from the open circuit potential (OCV) to 1.7 V, the LSV curves are shown in Fig. 6b. The Co-NCNTs@CNF-0.42 electrode has a prominent reduction peak at 1.95 V. In contrast, the reduction peak of the CP electrode is not apparent, indicating that the Co-NCNTs@CNF-0.42 electrode has catalytic activity, which can accelerate the reduction reaction of LiPSs compared with the CP electrode. When the voltage window varies from OCV to 2.8 V, the LSV curves are shown in Fig. 6c. The Co-NCNTs@CNF-0.42 electrode has two distinct oxidation peaks at 2.38 and 2.42 V, respectively. In contrast, an oxidation peak of the CP electrode appears at 2.58 V, indicating that the conversion from Li_2S_2/Li_2S to S_8 of the Co-NCNTs@CNF-0.42 electrode is faster than the CP electrode. As shown in Fig. 6d, the Tafel slope calculated from the Tafel plot of the Co-NCNTs@CNF-0.42 electrode (108 mV dec^{-1}) is much lower than that of the CP electrode (190 mV dec^{-1}), indicating that the Co-NCNTs@CNF-0.42 electrode has a faster reaction kinetics. Furthermore, according to Faraday's law,[66,67] the Li_2S precipitation area of Co-NCNTs@CNF-0.42 is larger than that of CP. Additionally, the nucleation response of Li_2S on Co-NCNTs@CNF-0.42 was earlier than CP, as shown in Fig. S17.† These results further suggest that the Co-NCNTs@CNF-0.42 electrode has catalytic activity, which contributes to accelerating the redox reaction kinetics of sulfur species. To better understand the reason for improved redox reaction kinetics of the Co-NCNTs@CNF-0.42, Gibbs free energies (ΔG) profiles of the last two steps of redox reaction in Li–S batteries (main rate-limited steps) [$*Li_2S_4 \rightarrow *Li_2S_2 + (1/4)S_8$ and $*Li_2S_2 \rightarrow *Li_2S + (1/8)S_8$] on CP and Co-NCNTs@CNF-0.42 substrates are calculated by using the DFT method. As displayed in Fig. 6e, one can see that the ΔG of Co-NCNTs@CNF-0.42 for the reduction of Li_2S_4* to Li_2S_2* and Li_2S_2* to Li_2S* is 0.52 and 0.69 eV, respectively, much lower than that of CP (1.02 and 1.07 eV), indicating that the reduction of S is much more favorable on Co-NCNTs@CNF-0.42 than on the CP substrate,[68] which highlights the catalytic effect of Co-NCNTs@CNF-0.42 on the conversion of LiPSs to Li_2S.

In situ XRD measurements were performed to study the phase transformation of sulfur species in the electrochemical reaction under a high sulfur loading of 6.0 mg cm^{-2}. As shown in Fig. S18,† during the discharge process, the peak detected at $2\theta = 23.5°$ belongs to α-S_8 (JCPDS No. 08-0247),[69] which decreases and disappears before the end of the high voltage plateau (2.3 V). This result corresponds to the solid–liquid two-phase transition in the reaction mechanism of Li–S batteries, followed by the liquid–liquid phase reaction. When approaching the low voltage plateau (2.1 V), a new peak starts to appear at 27°, which may be related to the formation of Li_2S (JCPDS No. 023-0369).[70] The *in situ* XRD result indicates that even at high sulfur loading, the Co-NCNTs@CNF-0.42-S cathode incorporated with an interlayer promotes the reversible transformation of α-S_8 to Li_2S, resulting in a higher discharge specific capacity (1330 mA h g^{-1}).

The *in situ* Raman spectroscopy test can monitor the redox reaction process of sulfur species during the charge–discharge process in real-time. Fig. 7 shows the time-resolved Raman images of the discharge and charge processes of Co-NCNTs@CNF-0.42-S cathode combined with Co-NCNTs@CNF-0.21 interlayer at different voltages. The *in situ* Raman battery was discharged and charged by the CV method. Since the battery was discharged to 1.7 V before the test, peaks at 373, 420, and 570 cm^{-1} were detected at the beginning of the charging process, which may correspond to $S_6^{2-} + S_8^{2-} + Li_2S$, S_6^{2-}, and $S_6^{2-} + Li_2S_2 + LiS_3\cdot$, respectively.[36,71] When the charging voltage was increased from 1.7 to 2.6 V, it was observed that the signal of S_6^{2-} was significantly weakened. The CV curve showed that the oxidation reaction was over (Fig. 7b), indicating that most of the LiPSs had been oxidized to S_8 or Li_2S_8, consistent with the Raman spectra. When the voltage approaches 1.8 V during the discharge process, the signal of $S_6^{2-} + Li_2S_2 + LiS_3\cdot$ gradually increases (Fig. 7c), indicating the continuous formation of Li_2S_2/Li_2S at this stage. When the voltage decreased from 2.6 to 1.7 V, the CV curve showed two reduction peaks at 2.30 and 1.95 V (Fig. 7d), respectively, corresponding to the reduction of long-chain Li_2S_8 to Li_2S_4 and Li_2S_2/Li_2S. Additionally, no more signal peaks were observed in the Raman spectra during the electrochemical reaction, indicating that the shuttle effect was

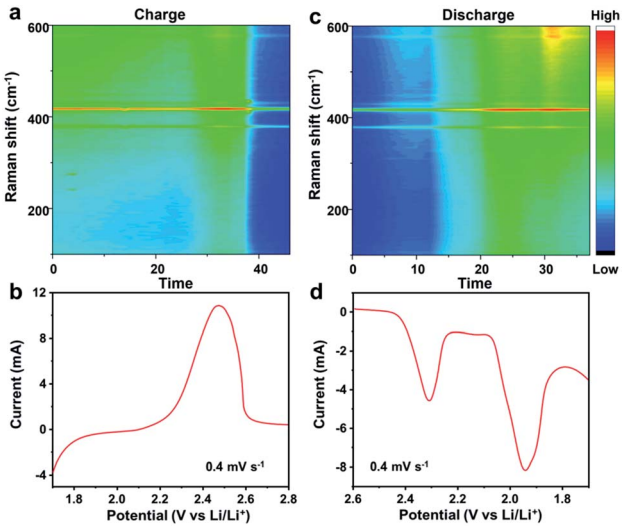

Fig. 7 (a and c) *In situ* time-resolved Raman spectra and (b and d) corresponding CV curves of Co-NCNTs@CNF-0.42-S electrode.

effectively inhibited due to the multiple roles of Co-NCNTs@CNF film.

Conclusions

In summary, a 3D carbon nanofiber film decorated with Co-N_x doped CNTs has been prepared using α-MnO_2 nanowires and Co-containing hydrotalcite, followed by a CVD method. Endowed with two functions as the sulfur host and an interlayer, Co-NCNTs@CNF film has the following advantages: (1) the interior of CNF has a multi-cavity structure, providing enough space for high loading and relieving the volume changes of sulfur. (2) *In situ* protruded CNTs and CNF can form a 3D conductive framework, conducive to accelerating the transfer of electrons and ions. (3) The introduction of Co-containing hydrotalcite contributes to forming a macroporous structure with an improved mesoporous ratio of the film, which is beneficial for electrolyte penetration, thereby reducing the E/S. (4) Co-N_x sites can act as high-efficiency adsorbents and catalysts to adsorb polysulfides and catalyze the conversion of polysulfides quickly. Owing to the synergistic effect, Co-NCNTs@CNF–0.42-S cathode combined with the interlayer delivers a high areal capacity of 4.77 mA h cm^{-2} at 0.2C after 100 cycles under high sulfur loading of 6.7 mg cm^{-2} and E/S = 10 μL mg^{-1}.

Conflicts of interest

There are no conflicts to declare.

Acknowledgements

This project was financially supported by the National Natural Science Foundation of China (Nos. 21776041 and 21875028), the Liao Ning Revitalization Talents Program (XLYC1902045), and the Dalian Science and Technology Innovation Fund (2020JJ26GX030).

Notes and references

1 P. G. Bruce, S. F. Freunberger, L. J. Hardwick and J.-M. Tarascon, *Nat. Mater.*, 2011, **11**, 19–29.
2 M. Zhao, B. Q. Li, X. Q. Zhang, J. Q. Huang and Q. Zhang, *ACS Cent. Sci.*, 2020, **6**, 1095–1104.
3 A. Bhargav, J. He, A. Gupta and A. Manthiram, *Joule*, 2020, **4**, 285–291.
4 Y.-C. Chien, M. J. Lacey, N.-J. Steinke, D. Brandell and A. R. Rennie, *Chem*, 2022, **8**, 1–17.
5 J. Lei, T. Liu, J. Chen, M. Zheng, Q. Zhang, B. Mao and Q. Dong, *Chem*, 2020, **6**, 2533–2557.
6 Z. Yu, M. Liu, D. Guo, J. Wang, X. Chen, J. Li, H. Jin, Z. Yang, X. Chen and S. Wang, *Angew. Chem., Int. Ed.*, 2020, **59**, 6406–6411.
7 R. Wang, J. Yang, X. Chen, Y. Zhao, W. Zhao, G. Qian, S. Li, Y. Xiao, H. Chen, Y. Ye, G. Zhou and F. Pan, *Adv. Energy Mater.*, 2020, **10**, 1903550.
8 J. Xu, W. Tang, C. Yang, I. Manke, N. Chen, F. Lai, T. Xu, S. An, H. Liu, Z. Zhang, Y. Cao, N. Wang, S. Zhao, D. Niu and R. Chen, *ACS Energy Lett.*, 2021, **6**(9), 3053–3062.
9 C.-Y. Chen, H.-J. Peng, T.-Z. Hou, P.-Y. Zhai, B.-Q. Li, C. Tang, W. Zhu, J.-Q. Huang and Q. Zhang, *Adv. Mater.*, 2017, **29**, 1606802.
10 X. Zhang, K. Chen, Z. Sun, G. Hu, R. Xiao, H.-M. Cheng and F. Li, *Energy Environ. Sci.*, 2020, **13**, 1076–1095.
11 S. Chen, J. Zhang, Z. Wang, L. Nie, X. Hu, Y. Yu and W. Liu, *Nano Lett.*, 2021, **21**, 5285–5292.
12 Z. Li, B. Y. Guan, J. Zhang and X. W. Lou, *Joule*, 2017, **1**, 576–587.
13 S. Z. Wang, S. P. Feng, J. W. Liang, Q. M. Su, F. P. Zhao, H. J. Song, M. Zheng, Q. Sun, Z. X. Song, X. H. Jia, J. Yang, Y. Li, J. X. Liao, R. Y. Li and X. L. Sun, *Adv. Energy Mater.*, 2021, **11**, 2003314.
14 T. Chen, Z. Zhang, B. Cheng, R. Chen, Y. Hu, L. Ma, G. Zhu, J. Liu and Z. Jin, *J. Am. Chem. Soc.*, 2017, **139**, 12710–12715.
15 H. He, Y. Liao, W. Zuo, G. Li, J. Gu, Y. Li, Z. Hu and Y. Yang, *Small*, 2021, **17**, 2103778.
16 Z. Shen, Z. Zhang, M. Li, Y. Yuan, Y. Zhao, S. Zhang, C. Zhong, C. Zhong, J. Zhu, J. Lu and H. Zhang, *ACS Nano*, 2020, **14**, 6673–6682.
17 Y. Yang, Y. Zhong, Q. Shi, Z. Wang, K. Sun and H. Wang, *Angew. Chem., Int. Ed.*, 2018, **57**, 15549–15552.
18 X.-F. Yu, D.-X. Tian, W.-C. Li, B. He, Y. Zhang, Z.-Y. Chen and A.-H. Lu, *Nano Res.*, 2019, **12**, 1193–1197.
19 L. Du, H. Wang, M. Yang, L. Liu and Z. Niu, *Small Struct.*, 2020, **1**, 2000047.
20 F. Ma, X. Zhang, K. Sriniva, D. Liu, Z. Zhang, X. Chen, W. Zhang, Q. Wu and Y. Chen, *J. Mater. Chem. A*, 2022, **10**, 8578–8590.
21 B. Liu, R. Fang, D. Xie, W. Zhang, H. Huang, Y. Xia, X. Wang, X. Xia and J. Tu, *Energy Environ. Mater.*, 2018, **1**, 196–208.
22 Z. Tong, L. Huang, H. Liu, W. Lei, H. Zhang, S. Zhang and Q. Jia, *Adv. Funct. Mater.*, 2021, **31**, 2010455.
23 Y. Pang, J. Wei, Y. Wang and Y. Xia, *Adv. Energy Mater.*, 2018, **8**, 1702288.
24 J. Xu, S. An, X. Song, Y. Cao, N. Wang, X. Qiu, Y. Zhang, J. Chen, X. Duan, J. Huang, W. Li and Y. Wang, *Adv. Mater.*, 2021, **33**, 2105178.
25 H. Yuan, J.-Q. Huang, H.-J. Peng, M.-M. Titirici, R. Xiang, R. Chen, Q. Liu and Q. Zhang, *Adv. Energy Mater.*, 2018, **8**, 1802107.
26 Q. Guo and Z. Zheng, *Adv. Funct. Mater.*, 2020, **30**, 1907931.
27 M. Zhao, H.-J. Peng, J.-Y. Wei, J.-Q. Huang, B.-Q. Li, H. Yuan and Q. Zhang, *Small Methods*, 2020, **4**, 1900344.
28 Y. Liu, Y. Elias, J. Meng, D. Aurbach, R. Zou, D. Xia and Q. Pang, *Joule*, 2021, **5**, 2323–2364.
29 W. Yan, J. Wei, T. Chen, L. Duan, L. Wang, X. Xue, R. Chen, W. Kong, H. Lin, C. Li and Z. Jin, *Nano Energy*, 2021, **80**, 105510.
30 H. F. Xu, Q. B. Jiang, B. K. Zhang, C. Chen and Z. Lin, *Adv. Mater.*, 2020, **32**, 1906357.
31 Z. Ye, Y. Jiang, L. Li, F. Wu and R. Chen, *Adv. Mater.*, 2020, **32**, 2002168.

32 Y. Fang, D. Luan, S. Gao and X. W. Lou, *Angew. Chem., Int. Ed.*, 2021, **60**, 20102.
33 R. Fang, S. Zhao, P. Hou, M. Cheng, S. Wang, H.-M. Cheng, C. Liu and F. Li, *Adv. Mater.*, 2016, **28**, 3374–3382.
34 L.-H. Zhang, B. He, W.-C. Li and A.-H. Lu, *Adv. Energy Mater.*, 2017, **7**, 1701518.
35 X.-F. Yu, W.-C. Li, Y.-R. Hu, C.-Y. Ye and A.-H. Lu, *Nano Res.*, 2021, **14**, 1565–1573.
36 R. Hou, S. Zhang, Y. Zhang, N. Li, S. Wang, B. Ding, G. Shao and P. Zhang, *Adv. Funct. Mater.*, 2022, 2200302.
37 L. Peng, Z. Wei, C. Wan, J. Li, Z. Chen, D. Zhu, D. Baumann, H. Liu, C. S. Allen, X. Xu, A. I. Kirkland, I. Shakir, Z. Almutairi, S. Tolbert, B. Dunn, Y. Huang, P. Sautet and X. Duan, *Nat. Catal.*, 2020, **3**, 762–770.
38 Z. Zhang, L.-L. Kong, S. Liu, G.-R. Li and X.-P. Gao, *Adv. Energy Mater.*, 2017, **7**, 1602543.
39 B. He, W.-C. Li, Y. Zhang, X.-F. Yu, B. Zhang, F. Li and A.-H. Lu, *J. Mater. Chem. A*, 2018, **6**, 24194–24200.
40 N. Wang, X. Zhang, Z. Ju, X. Yu, Y. Wang, Y. Du, Z. Bai, S. Dou and G. Yu, *Nat. Commun.*, 2021, **12**, 4519.
41 J. L. Guo, H. Y. Pei, Y. Dou, S. Y. Zhao, G. S. Shao and J. P. Liu, *Adv. Funct. Mater.*, 2021, **31**, 2010499.
42 W. Yao, C. Tian, C. Yang, J. Xu, Y. Meng, I. Manke, N. Chen, Z. Wu, L. Zhan, Y. Wang and R. Chen, *Adv. Mater.*, 2022, **34**, 2106370.
43 Y. Xie, G. Pan, Q. Jin, X. Qi, T. Wang, W. Li, H. Xu, Y. Zheng, S. Li, L. Qie, Y. Huang and J. Li, *Adv. Sci.*, 2020, **7**, 1903168.
44 S.-H. Chung and A. Manthiram, *Adv. Mater.*, 2018, **30**, 1705951.
45 Y. Yoshie, K. Hori, T. Mae and S. Noda, *Carbon*, 2021, **182**, 32–41.
46 B. Lan, L. Yu, T. Lin, G. Cheng, M. Sun, F. Ye, Q. Sun and J. He, *ACS Appl. Mater. Interfaces*, 2013, **5**, 7458–7464.
47 G. Kresse and J. Hafner, *Phys. Rev. B*, 1994, **49**, 14251–14269.
48 G. Kresse and J. Hafner, *Phys. Rev. B*, 1993, **47**, 558–561.
49 P. E. Blöchl, *Phys. Rev. B*, 1994, **50**, 17953–17979.
50 G. Kresse and D. Joubert, *Phys. Rev. B*, 1999, **59**, 1758–1775.
51 G. Kresse and J. Hafner, *Phys. Rev. B*, 1993, **48**, 13115–13118.
52 J. P. Perdew, K. Burke and M. Ernzerhof, *Phys. Rev. Lett.*, 1996, **77**, 3865–3868.
53 S. Grimme, J. Antony, S. Ehrlich and H. Krieg, *J. Chem. Phys.*, 2010, **132**, 154104.
54 S. Zhang, Y. Zhang, W. J. Jiang, X. Liu, S. Xu, R. Huo, F. Zhang and J.-S. Hu, *Carbon*, 2016, **107**, 162–170.
55 L. Song, H. Fan, T. Wang, T. Xiang, M. Zhang, C. Hu, W. Zhou and J. He, *Energy Storage Mater.*, 2021, **43**, 365–374.
56 Y. Chen, C. Jing, X. Zhang, D. Jiang, X. Liu, B. Dong, L. Feng, S. Li and Y. Zhang, *J. Colloid Interface Sci.*, 2019, **548**, 100–109.
57 J. Zhou, C. Tang, B. Cheng, J. Yu and M. Jaroniec, *ACS Appl. Mater. Interfaces*, 2012, **4**, 2174–2179.
58 Y. Li, C. Zhong, J. Liu, X. Zeng, S. Qu, X. Han, Y. Deng, W. Hu and J. Lu, *Adv. Mater.*, 2018, **30**, 1703657.
59 T. Liu, J. Mou, Z. Wu, C. Lv, J. Huang and M. Liu, *Adv. Funct. Mater.*, 2020, **30**, 2003407.
60 Z. Yang, C. Zhao, Y. Qu, H. Zhou, F. Zhou, J. Wang, Y. Wu and Y. Li, *Adv. Mater.*, 2019, **31**, 1808043.
61 H.-W. Liang, S. Brüller, R. Dong, J. Zhang, X. Feng and K. Müllen, *Nat. Commun.*, 2015, **6**, 7992.
62 X. Yang, G. Xia, J. Ye, W. Du, Z. Zheng, A. Zhang, X. Li, C. Chen and C. Hu, *Appl. Surf. Sci.*, 2021, **541**, 148632.
63 D. Wang, K. Ma, J. Hao, W. Zhang, C. Wang, C. Xu, H. Shi, Z. Ji, X. Yan and Y. Gu, *Nano Energy*, 2021, **89**, 106426.
64 X.-F. Yu, W.-C. Li, B. He, L. Shi, F. Tang, D. Yan, D. Wang and A.-H. Lu, *Chem. Eng. J.*, 2022, **430**, 132987.
65 Y. Yang, Y. Zhong, Q. Shi, Z. Wang, K. Sun and H. Wang, *Angew. Chem., Int. Ed.*, 2018, **57**, 15549–15552.
66 F. Y. Fan, W. C. Carter and Y.-M. Chiang, *Adv. Mater.*, 2015, **27**, 5203–5209.
67 W. Yao, W. Zheng, J. Xu, C. Tian, K. Han, W. Sun and S. Xiao, *ACS Nano*, 2021, **15**, 7114–7130.
68 Z. Du, X. Chen, W. Hu, C. Chuang, S. Xie, A. Hu, W. Yan, X. Kong, X. Wu, H. Ji and L.-J. Wan, *J. Am. Chem. Soc.*, 2019, **141**, 3977–3985.
69 J. Nelson, S. Misra, Y. Yang, A. Jackson, Y. Liu, H. Wang, H. Dai, J. C. Andrews, Y. Cui and M. F. Toney, *J. Am. Chem. Soc.*, 2012, **134**, 6337–6343.
70 X. C. Liu, Y. Yang, J. Wu, M. Liu, S. P. Zhou, B. D. A. Levin, X. D. Zhou, H. Cong, D. A. Muller, P. M. Ajayan, H. D. Abruña and F. S. Ke, *ACS Energy Lett.*, 2018, **3**, 1325–1330.
71 G. Zeng, Y. Liu, D. Chen, C. Zhen, Y. Han and W. He, *Adv. Energy Mater.*, 2021, **11**, 2102058.